

## Slip Sequences in Laboratory Experiments Resulting from Inhomogeneous Shear as Analogs of Earthquakes Associated with a Fault Edge

SHMUEL M. RUBINSTEIN,<sup>1</sup> ITAY BAREL,<sup>2</sup> ZE'EV RECHES,<sup>3</sup> OLEG M. BRAUN,<sup>4</sup> MICHAEL URBAKH,<sup>2</sup> and JAY FINEBERG<sup>1</sup>

**Abstract**—Faults are intrinsically heterogeneous with common occurrences of jogs, edges and steps. We therefore explore experimentally and theoretically how fault edges may affect earthquake and slip dynamics. In the presented experiments and accompanying theoretical model, shear loads are applied to the edge of one of two flat blocks in frictional contact that form a fault analog. We show that slip occurs via a sequence of rapid rupture events that initiate from the loading edge and are arrested after propagating a finite distance. Each successive event extends the slip size, transfers the applied shear across the block, and causes progressively larger changes of the contact area along the contact surface. Resulting from this sequence of events, a hard asperity is dynamically formed near the loaded edge. The contact area beyond this asperity is largely reduced. These sequences of rapid events culminate in slow slip events that precede a major, unarrested slip event along the entire contact surface. We suggest that the 1998 M5.0 Sendai and 1995 off-Etorofu earthquake sequences may correspond to this scenario. Our work demonstrates, qualitatively, how the simplest deviation from uniform shear loading may significantly affect both earthquake nucleation processes and how fault complexity develops.

### 1. Introduction

Faults are commonly modelled as planar interfaces separating two elastic half-spaces which are driven by a spatially uniform shear that is imposed by the motion of tectonic plates (DAS, 2003; LAPUSTA and RICE, 2003; LAPUSTA *et al.*, 2000; RICE and BEN-ZION, 1996). Numerous natural faults, however, are loaded

by a superposition of the uniform shear due to remote loading (e.g., plate motion), and highly nonuniform loading generated by local fault heterogeneities (e.g. steps, jogs, asperities and edges) (BEN-ZION and SAMMIS, 2003; HARRIS and DAY, 1993; SHAW and DIETERICH, 2007; WESNOUSKY, 2006) that are abundant along fault-zones. This complexity may govern some earthquake properties.

Configurations in which edge-loading may play an important role are common along active faults in the earth's crust, and include: slip along a segment within a long fault that loads the neighbouring segments at the edge of the slipped region (e.g. north Anatolian fault (STEIN *et al.*, 1997), the physical edges formed between abutting segments (e.g. the intersection of the Susitna Glacier and Denali faults (AAGAARD and HEATON, 2004), and by asperities and steps along fault strands (HARRIS and DAY, 1993; JOHNSON *et al.*, 1994; LAY *et al.*, 1982; SAGY *et al.*, 2007; SHAW and DIETERICH, 2007; WESNOUSKY, 2006). As these examples show, the loading of large crustal faults is frequently modelled by a combination of “basal loading” on the crust base, and “edge loading” at the fault edge (LACHENBRUCH and SASS, 1980; MATSUURA and SATO, 1997; RECHES *et al.*, 1994).

In this paper we explore both experimentally and theoretically the influence of one specific type of nonuniformity that results when shear loading is applied to a fault's edge. Our laboratory “fault” is formed by two elastic blocks, a base and a slider (Fig. 1), separated by a roughened, but perfectly planar, frictional interface. Shear force is applied to one edge of the slider block while a uniform normal stress is remotely applied. This loading configuration is an idealized model for the inhomogeneous loading that may occur at an edge or asperity along an otherwise planar fault. To highlight the unique

<sup>1</sup> The Racah Institute of Physics, The Hebrew University of Jerusalem, Givat Ram, 91904 Jerusalem, Israel. E-mail: jay@vms.huji.ac.il

<sup>2</sup> The School of Chemistry, Tel Aviv University, 69978 Tel Aviv, Israel.

<sup>3</sup> School of Geology and Geophysics, University of Oklahoma, Norman, OK 73019, USA.

<sup>4</sup> Institute of Physics, National Academy of Sciences of Ukraine, Kiev 03028, Ukraine.

contributions of the nonuniform application of shear to the resulting fault dynamics, our model focuses on the effects of the nonuniform component and ignores the uniform component of the applied shear.

The experimental system is simulated by a spring-slider equivalent (Fig. 2). A slider of total mass  $M$  moves over an immobile rigid substrate (the base) and is pushed from its trailing edge (the left side) with a constant velocity  $V_d$  through a spring of elastic constant  $K_d$ . The force,  $F$ , applied to the spring equals the frictional force and is continuously monitored throughout the simulation. The elasticity of the slider is incorporated by splitting it into  $N$  rigid blocks, which are coupled by a second set of springs with an elastic constant  $K_b = (N - 1)K$  so that the slider rigidity is  $K$ . This approach is similar to that proposed in the Burridge–Knopoff spring-block model of earthquakes (BURRIDGE and KNOPOFF, 1967), which has been further developed in a number of studies (CARLSON and LANGER, 1989; OLAMI *et al.*, 1992). However, contrary to most earthquake models where phenomenological laws have been introduced to describe friction at the slider-base interface, here we explicitly include interactions between each slider's block and the base through an array of "surface contacts", which represent interfacial asperities (BAREL *et al.*, 2010; BRAUN *et al.*, 2009; BRAUN and RÖDER, 2002; FILIPPOV *et al.*, 2004; PERSSON, 1995). This model enables us not only to explain experimental observations but also to predict the effect of material

properties on the dynamics of the transition to sliding in this type of loading configuration.

## 2. Methods

### 2.1. Experimental Methods

The experimental setup used is described in detail in (RUBINSTEIN *et al.*, 2004, 2006). We performed real-time measurements of the true area of contact,  $A(x, y, t)$ , along the entire interface separating two polymethyl-methacrylate (PMMA) blocks whose ( $x$ : $y$ : $z$ ) dimensions were 300:30:27 mm for the static ("base") block and either 140:6:75 mm or 200:6:75 mm for sliding ("slider") block.  $x$ ,  $y$ , and  $z$  are, respectively, the sliding, sample width, and normal loading directions. The initially optically flat base-slider interface was roughened to 1  $\mu\text{m}$  rms. For the range ( $1 < F_N < 4$  kN) of normal load ( $F_N$ ) applied,  $A(x, y, t)$  varied from 0.35 to 1.35% of the interface's nominal contact area (DIETERICH and KILGORE, 1994).  $A(x, y, t)$  was measured by illuminating the contact area by a sheet of laser light whose incident angle was far below the critical angle for total internal reflection from the PMMA-air layer within the rough interface. Thus light is transmitted only at points of contact, with an intensity at each point ( $x, y$ ) proportional to  $A(x, y, t)$ . Using a high-speed camera, we imaged  $A(x, y, t)$  at rates up to 100,000 frames/s. The data acquisition was designed to capture both slow processes at the quasi-static time scales governed by the loading rate and rapid, rupture processes whose entire duration takes place in the sub-msec range. As the onset dynamics are governed by one-dimensional rupture fronts (RUBINSTEIN *et al.*, 2004),  $A(x, y, t)$  was averaged in  $y$ , yielding  $A(x, t)$  to 1,280 pixel resolution. Thus,  $A(x, t)$  provides a local measurement of the contact area, where each pixel measures the integrated contact area a  $0.1 \times 6$  mm region (with the higher resolution in the direction of motion). At the initiation of each experiment, before the application of shear, the slider was oriented relative to the base to form an initial contact area that was, statistically, spatially uniform (utilizing the  $A(x, y)$  measurements to guide the positioning). Upon completion of this initial positioning,  $F_N$  was uniformly applied. The corresponding

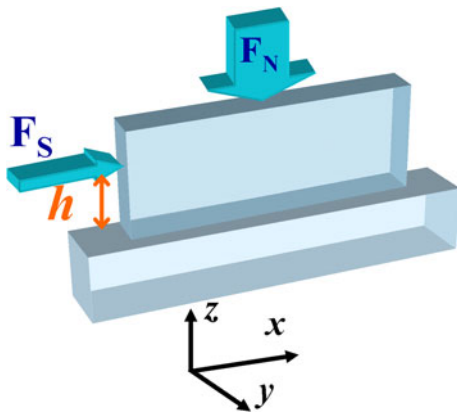


Figure 1

A schematic illustration of the base and slider blocks and load application

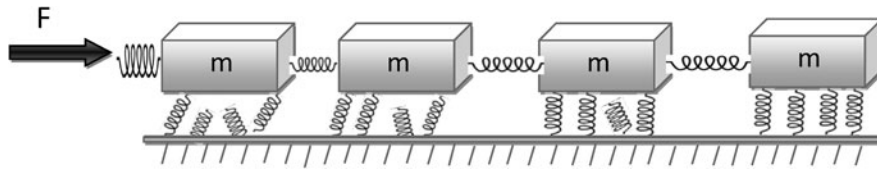


Figure 2  
Schematic sketch of a model setup

value of  $A(x, t = 0)$  was then used to normalize subsequent measurements of  $A(x, t)$  to allow us to measure the changes in  $A(x, t)$  resulting from the dynamics at each point  $x$ .

At  $t = 0$ , a shear force,  $F_S$ , was applied in the  $x$  direction to one edge (the “trailing” edge at  $x = 0$ ) of the slider at a height  $z = h$  ( $2 < h < 18$  mm) above the interface (see Fig. 1).  $F_S$  was increased from zero at a constant rate (ranging from 1 to 20  $\mu\text{m/s}$ ) until, at  $F_S = \mu_S F_N$ , stick–slip sliding initiated. As long as  $h$  was defined as the mean height of the applied shear force, the precise means by which  $F_S$  was applied was unimportant (e.g. via rigid blocks of various dimensions). In this loading system (RUBINSTEIN *et al.*, 2007, 2008, 2009), any slip of the trailing edge immediately results in a sharp drop of  $F_S$ , which corresponds to the trailing edge of the slider “outrunning” the actuator that applied the shear force. While the leading edge (at  $x = L$ ) is stationary, drops of  $F_S$  mirror the stress release across the interface.

## 2.2. Simulation Procedure

Behavior of a single block interacting with a base block through an array of surface contacts has been studied previously (BAREL *et al.*, 2010; BRAUN and PEYRARD, 2008; BRAUN and TOSATTI, 2009; FILIPPOV *et al.*, 2004). Here we focus on the collective motion of the chain of elastically interacting blocks. Each contact connects the block and the base through a spring with an elastic constant  $k_i$ , where  $i = 1, 2, \dots, N_s$  and  $N_s$  is the number of contacts between the block and base. The frictional dynamics are governed by two competing processes: (1) formation of contacts (junctions) between the block and the base that tend to inhibit sliding, and (2) rupture of contacts, i.e., detachment of springs from the block, a process that

promotes sliding. So long as a contact is intact, the contact’s spring elongates or shortens with the velocity of the corresponding block. Therefore, the interface applies a force on each block of  $-f = \sum_i^{N_s} f_i$ , where  $f_i = k_i l_i$  and  $l_i(t)$  is the spring length. Additionally, this force is supplemented by the elastic forces acting from both the left and right neighboring blocks.

To complete the description of the local block dynamics, we must specify the laws that govern the rupture and formation of contacts. We assume that as long as the force,  $f_i$ , is below a certain threshold,  $f_{si}$ , which models either plastic flow of the contacting asperities or local melting of the boundary lubrication layer, this contact moves together with the corresponding block. When the force exceeds this threshold, the contact detaches from the slider, and reattaches to the block in an unstressed state (i.e., with the length  $l_i = 0$ ) after some delay time,  $\tau$ . The threshold value,  $f_{si}$ , of each contact is assigned a random value from a Gaussian distribution having a mean value  $f_s = f_s / (NN_s)$  and a standard deviation  $\Delta f_s$ , where  $NN_s$  is a total number of contacts between the slider and base. We note that  $f_{si}$  is proportional to the area  $A_i$  of a given contact, while the transverse rigidity  $k_i$  is proportional to the contact’s size,  $k_i \propto \sqrt{A_i}$ . The distribution of contact’s spring constants is, therefore, coupled to the distribution of threshold forces by the relation  $k_i = \langle k \rangle (f_{si}/f_s)^{1/2}$ , where  $\langle k \rangle$  is the mean value of the contact spring constants. When a contact reattaches to the slider, it is assigned new values of the parameters,  $f_{si}$  and  $k_i$ . The model can be easily generalized to include aging of the contacts by specifying a dependence of  $f_{si}$  on the lifetime of the contact.

The mechanism of contacts detachment assumed in our model is similar to that proposed previously by the fiber bundle models (ALAVA *et al.*, 2006).

However, here the coupling between the applied force and the detachment and reattachment processes are different from the coupling considered in the fiber bundle models, and in particular in the fiber bundle model with equal load sharing. As a result the dynamical response of our system differs significantly from that predicted by the fiber bundle models.

Artificial vibrations of the blocks are avoided by the introduction of a viscous damping force with a coefficient  $\eta$  for the block motion relative to the base,  $f_\eta = -m\eta\dot{x}_j$ , where  $x_j$  is the center of mass coordinate of the  $j$ -th block and  $m = M/N$  is its mass. We note that the block's oscillations may also be damped due to internal friction within the blocks, i.e., due to phonon excitations inside the slider. The results of our simulations show that the dynamics of transition to sliding are insensitive to any particular choice of the damping force.

We performed calculations over a wide range of the model parameters. Here, however, we present results only for a particular set of parameters:  $K_d = 4 \times 10^6$  N/m,  $M = 11.5$  kg,  $F_s = 3.0 \times 10^3$  N,  $K = 1.56 \times 10^7$  N/m,  $V_d = 0.3$  mm/s and  $\eta = 3.45 \times 10^4$  s<sup>-1</sup>,  $\Delta f_s/f_s = 0.05$ ,  $\tau = 0.005$  s. The values of the macroscopic parameters,  $K_d$ ,  $M$ ,  $F_s$ ,  $K$  and  $V_d$  were chosen to model the experimental conditions. Knowing Young's modulus,  $E$ , of the slider, its length,  $L$ , and the cross-sectional area,  $A$ , the elastic constant can be calculated as  $K = EA/L$ . As for the interface rigidity,  $K_s = N_s\langle k \rangle$ , we present results for two cases: (1) a soft interface with  $K_s = K$  (Fig. 7) and (2) a stiff interface with  $K_s = 50K$  (Fig. 10). The interface stiffness and mean rupture threshold force are expected to be directly related to the applied normal load. Most simulations were performed for seventy blocks ( $N = 70$ ) with 100 contacts between each block and the base ( $N_s = 100$ ).

### 3. Results

#### 3.1. Slip Sequences and Stress History

Concurrent measurements of contact area  $A(x, t)$ , and shear load  $F_S(t)$  for a typical experiment (Fig. 3) reveal that large, system sized, stick–slip events are the culmination of a complex history of precursory

slip events. The  $F_S(t)$  curve in Fig. 3 reveals a discrete sequence of small sharp stress drops that occur at stress levels well below the peak values of  $F_S(t)$  associated with the static friction coefficient ( $\mu_s \sim 0.4$  for PMMA). These small stress drops (of  $\sim 0.01$ – $0.02 F_S$ ) result from the propagation of a sequence of rapid arrested slip events. In the short-time measurements of  $A(x, t)$  (Fig. 4a) we observe that the initial slip events always initiate at the system's trailing edge, and propagate at “sub-Rayleigh” speeds, typically between 60 and 80% of the Rayleigh wave speed ( $V_R$ ), before abruptly arresting (Fig. 4). These initial events (Fig. 3, top) are associated with slipping segments of length  $l$  that are relatively small compared to the entire fault size,  $L$ . We find that  $l$  obeys a linear scaling relation (RUBINSTEIN *et al.*, 2007),  $l \propto F_S L/F_N$  (Fig. 5a). Such precursory behaviour together with linear scaling of the precursor length with  $F_S$  was recently observed in additional experiments under similar loading conditions (MAEGAWA *et al.*, 2010). This behaviour is also reminiscent of the step-like structure of the loading curves (c.f. Figs. 3, 6b) that are observed in simulations of precursory slip “avalanches” triggered by shear-induced deformation of solids (DAHMEN *et al.*, 2009; TSAMADOS *et al.*, 2008). Once  $l$  approaches  $0.4$ – $0.5 L$ , this scaling breaks down and the initial dynamics undergo a qualitative change that denotes a transition (RUBINSTEIN *et al.*, 2004; RUBINSTEIN *et al.*, 2006) to a new stage of dynamics. Here, the slip events also initiate at the trailing edge as rapid sub-Rayleigh slip events, but do not simply arrest. Instead, these larger events trigger the propagation of a “slow” front that propagates over a range of speeds ( $\sim 50$  m/s in Fig. 4b) that are slower than the sub-Rayleigh velocities of the triggering events by more than an order of magnitude (BEN-DAVID *et al.*, 2010a; NIELSEN *et al.*, 2010; RUBINSTEIN *et al.*, 2004, 2007, 2008). These slow fronts propagate stably for some time, and either traverse the remainder of the interface or transition back to sub-Rayleigh fronts, as shown in Fig. 4a (bottom). Significantly, overall motion (sliding) between the blocks initiates only after either a slow or subsequently triggered sub-Rayleigh front has reached the leading edge.

The discrete sequence of such arrested slip events, described by Fig. 3, is observed only when shear is imposed at the sample's trailing edge. It is not

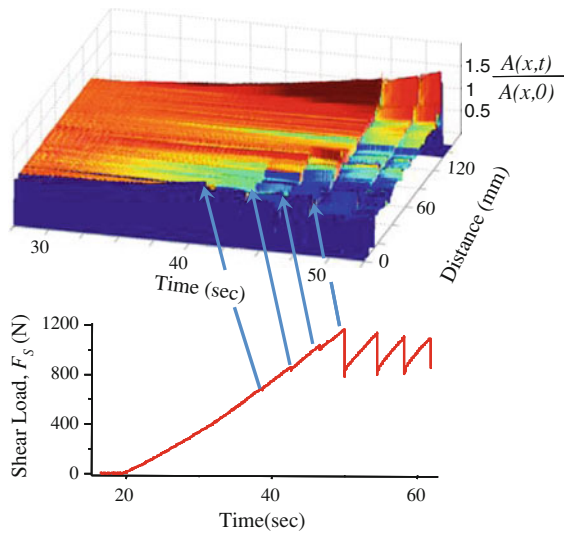


Figure 3

The transition to (stick–slip) sliding is preceded by a sequence of discrete arrested slip events. *Bottom* Applied shear force,  $F_S$ , as a function of time with the (*top*) corresponding spatio-temporal evolution of  $A(x, t)$ . Each small discrete drop in  $F_S$  corresponds to a rapid slip event that arrests within the interface. Each arrested slip event generates significant changes in  $A(x, t)$ . Arrested events, together with the corresponding drop in shear load, are denoted by the arrows. The large stress drops mark stick–slip motion. Interface length,  $L = 140$  mm,  $F_N = 3.3$  kN

observed when, for example, a uniform shear stress is imposed at a remote boundary parallel to the interface. With the trailing edge loading, each sequence initiates via a slip event of finite length,  $l_0$ , with  $l$  increasing by discrete increments,  $\Delta l$ , of constant length for each successive slip.

Figure 5b shows that the size of both  $l_0$  and  $\Delta l$  is proportional to  $h$ , the height above the interface where  $F_S$  is applied at the edge. Note that  $h$ , however, has no effect on the overall scaling of  $l$  (Fig. 5a). Since  $l$  scales linearly with  $F_S$ , the fixed value of  $\Delta l$  (for a given  $h$ ) indicates that slip events occur at fixed intervals,  $\Delta F_S$ , in  $F_S$ . Thus,  $h$ , which determines  $\Delta l$ , governs also the magnitude of the force drop intervals,  $\Delta F_S$ , between successive events. For a constant shear loading rate, (as in our experiments) the temporal periods between events are proportional to  $h$ .

### 3.2. Contact Area and Fault Strength

We now consider the evolution of the contact area  $A(x, t)$ . Prior to the first event,  $A(x, t)$  is spatially

uniform. The passage of each successive precursory slip event (Fig. 6) significantly alters the contact area, and hence changes the local fault strength. With each successive event, the contact area increases in a region of width  $D$ , which is adjacent to the sample's trailing edge. Thus, this process dynamically forms an asperity [a localized area whose resistance to slip is much greater than its surroundings (LAY *et al.*, 1982)]. Although this asperity continuously strengthens with  $F_S$  (Fig. 6b), its size,  $D$ , remains nearly constant throughout each experiment.

After overcoming this asperity, each slip both extends the length of the reduced contact area region created by its predecessors and further reduces  $A(x, t)$  by a significant amount. This systematic decrease of  $A(x, t)$  creates a highly weakened region ahead of the asperity. As a result of this process, by the time large-scale overall motion (stick–slip) occurs, the established contact profile is highly nonuniform. As shown in Fig. 6c, changes in  $h$  do not qualitatively affect the general shape of the contact area profiles. Quantitative analysis reveals, however (Fig. 6d), that the size of  $D$  is proportional to  $h$ . Figure 6d also demonstrates that both the height,  $G$ , of the asperity and relative weakening along the interface beyond the asperity [the reduction in  $A(x)$ ] appear to systematically decrease as  $h$  is increased.

One may suspect that the variations of the contact area is due to the torque imposed by  $F_S$ , as  $F_S$  is applied at a finite height  $h$  rather than at  $h = 0$ . We find that this effect is negligible over the range of used  $h$ . For example, the torque resulting from  $h = 2$  mm yields only a 3% variation of the normal stress over the interface length, whereas  $A(x, t)$  varies by over 50% (Fig. 6). In addition the effect of the applied torque (BEN-DAVID *et al.*, 2010a) is mainly concentrated on a sharp increase of  $A(x)$  at the leading edge (note the sharp rise of  $A(x)$  at  $x \sim 140$  mm in Fig. 6a, c).

Surprisingly, once a contact profile is created, it is retained by the system, remaining nearly unchanged both after large-scale slip and in successive stick–slip events (RUBINSTEIN *et al.*, 2007). Large residual stresses are, therefore, also retained even after system size slip events occur. As the contact area mirrors the normal stress values, the existence of this nonuniform profile also indicates that the normal stresses along

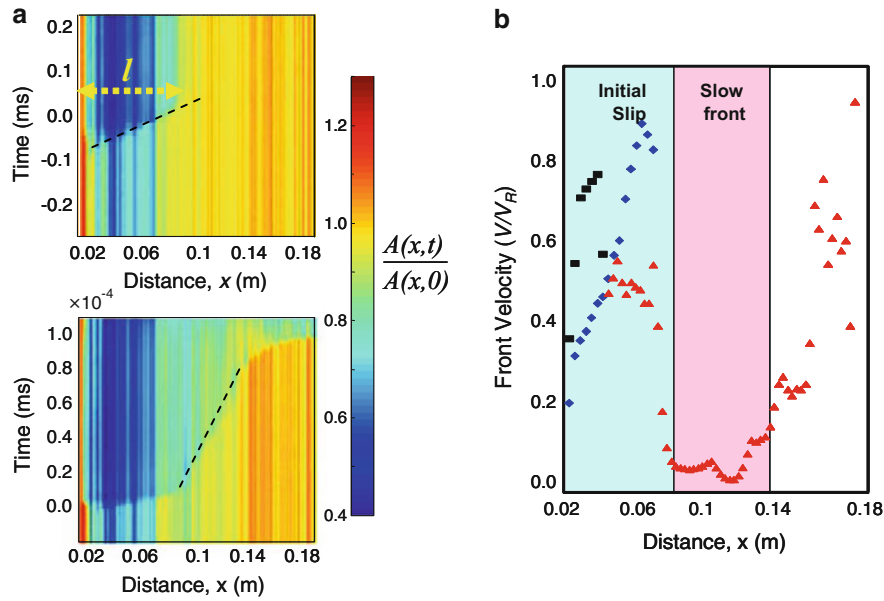


Figure 4

**a** Time-distance maps of the normalized contact area (*scale bar*) during slip events across the 0.18 m long experimental fault. *Top* an arrested slip event of length,  $l$ , generated at stresses well below the onset of stick–slip. *Bottom* the transition to stick–slip motion at the peak value of  $F_S$ . Here rapid slip arrests and triggers a slow front. At  $x = 0.14$  m the slow front nucleates a rapid slip that traverses the remainder of the interface. *Color bar* indicates the change in  $A(x, t)$ , relative to the initial, uniform value  $A(x, t = 0)$  when  $F_S = 0$ .  $A(x, t)$  measured at 14  $\mu$ s intervals in two different events. **b** The slip propagation velocities (as a function of  $x$ ) of arrested events (*diamonds* and *squares*) and the transition (*triangles*) to stick–slip motion. Velocities are determined from the slope of the event fronts (*dashed lines* in **a**). Events depicted by *diamonds* and *triangles* correspond to **a**

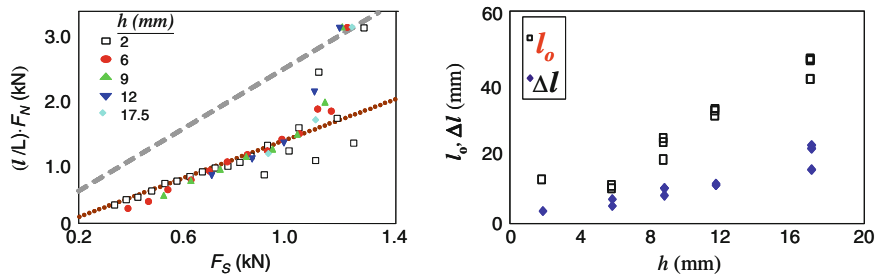


Figure 5

Scaling behaviour of the lengths  $l$  of successive slip events. **a**  $l/L F_N$  as a function of  $F_S$ , where  $F_S$  was applied at different heights,  $h$ , above the interface.  $h$  does not influence the  $l \propto L F_S / F_N$  scaling (RUBINSTEIN *et al.*, 2007) (*dotted line*). Here,  $F_N = 3$  kN and  $L = 140$  mm. This scaling breaks down at the transition to large events leading to stick–slip motion, described by the Amontons–Coulomb law (*dashed line*). **b** The values of both the initial slip length,  $l_0$  (*squares*), and the incremental extension of each slip event,  $\Delta l$  (*diamonds*), increase linearly with  $h$ .  $l_0$  saturates at low  $h$  suggesting that a minimal length is needed for development of instability. Different points at the same  $h$  correspond to different  $F_N$

the interface (or fault) are highly nonuniform. In particular, the normal stresses along significant regions of the interface are considerably weaker than the mean.

Why do the contact profiles remain frozen far from their equilibrium state? Once local slip has

ceased each point along the interface is pinned by frictional forces (BEN-DAVID *et al.*, 2010b). This pinning freezes the value of  $A(x, t)$  until the next rupture front enables local slip to take place. The reason for this is that, when slip occurs, each point along its path is locally freed by the rupture front. At

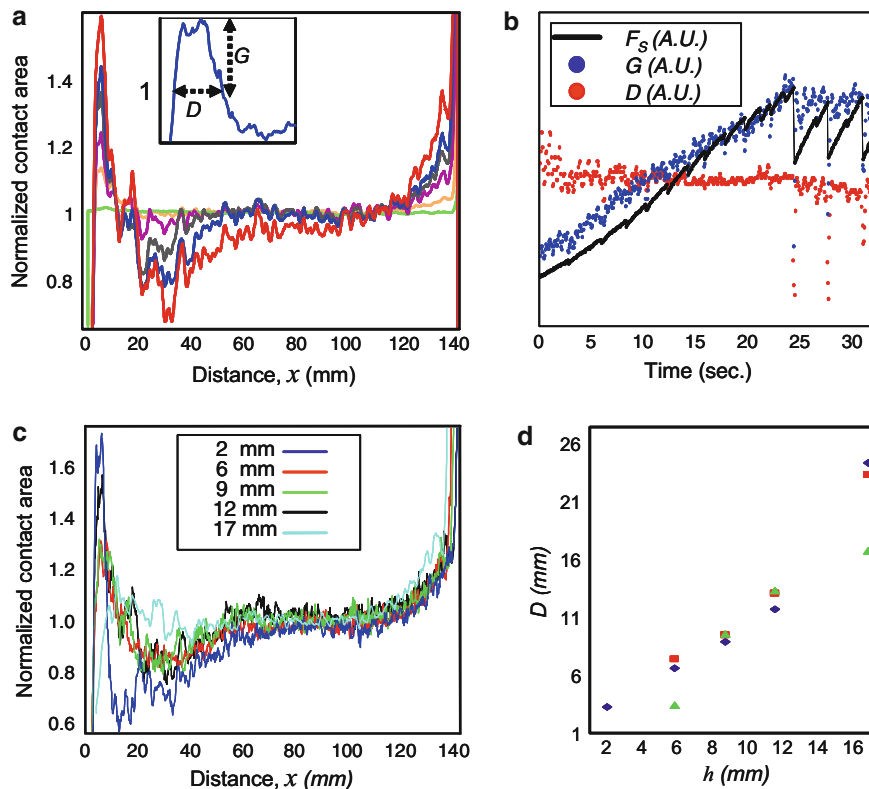


Figure 6

Evolution of the true contact area profile. **a**  $A(x, t)$  profiles formed by consecutive slip events of increasing length during a single whole stick-slip cycle. Deformations of the initially uniform contact profile are both amplified and extended with each slip. *Inset* Close-up of  $A(x, t)$  profile adjacent to the trailing edge depicting the width  $D$  and strength  $G$  of the asperity that is spontaneously formed there. **b**  $F_s$ ,  $D$  and  $G$  as a function of time for the experiment shown in **a**.  $F_s$ ,  $D$  and  $G$  are in arbitrary units to facilitate comparison. The asperity width  $D$ , stays nearly constant while  $G$  increases monotonically with  $F_s$ . **c**  $A(x, t)$  in experiments where  $h$  was varied. The profiles are qualitatively similar in appearance. **d**  $D$ , increases nearly linearly with  $h$ . All profiles in **c** were obtained for  $F_s$  at 75% of the value needed for the onset of stick-slip.  $A(x, t)$  in **a** and **c**, is normalized with respect to its spatially uniform value,  $A(x, t = 0)$ , at the start of the experiment

the same time, all of the points ahead and points sufficiently behind the tip of the front (BEN-DAVID *et al.*, 2010b) (where slip has arrested) remain pinned. As a result all of the contact points along the entire block are never simultaneously free to relax to their equilibrium position. For this reason, the blocks are constrained to their “distorted” state. This pinning occurs both during precursory slip events and large-scale events when the entire interface slips.

### 3.3. Simulations

We start our simulations in the state where the slider is unstressed, all surface contacts are intact and the entire interface is pinned. When the force is applied to the trailing edge of the slider, the shear

stress accumulates in a finite region near the loading point. The solution of 1D elastic equations shows that displacements of the blocks,  $x_j$ , from their equilibrium positions,  $x_j^0$ , and the corresponding contractions of the springs connecting the blocks,  $x_j - x_{j+1}$ , decrease exponentially with the distance from the trailing edge,  $x_0$ , namely  $x_j - x_j^0 \propto \exp[-\sqrt{K_s/NK}j]$ . Thus, the length of the stressed region is determined by the ratio of the contact and slider stiffnesses,  $K_s/K$ . The exponential distribution of the shear stress along the slider is characteristic for the 1D model employed here, while a 3D description of the slider leads to a power law decrease of the stress (LANDAU and LIFSHITZ, 1986). Nevertheless, the localization of the shear stress in a finite range at the trailing edge that results from the 1D description is consistent with our

experimental configuration where the finite spatial extent of the stressed region is determined by a height at which the force is applied.

Applying load at the height  $h$  from the interface may lead to a nonuniform distribution of the normal load along the slider that can be taken into account by introducing a corresponding nonuniform distribution of the number of contacts along the chain of blocks. Recently the effect of nonuniform normal loading on frictional motion has been simulated within a slider-block model by introducing a distribution of static friction forces along the slider (MAEGAWA *et al.*, 2010). It has been found that this effect influences a length and number of precursors but does not change the qualitative conclusions of the work.

In order to provide an accurate description of the continuum system within the framework of the slider-block model, the number of blocks should be large enough so that the decay length of the stress distribution,  $\sqrt{NK/K_s}$ , is larger than one. Under this condition, the results of simulations are independent of the number of blocks (for given values of  $M$  and  $K$ ).

As the applied force is increased, the stress in this region grows until it exceeds the thresholds for the rupture of surface contacts,  $f_{si}$ , and a detachment front starts to propagate across the interface (see Fig. 7). The manifestation of the detachment fronts is seen in the loading curves,  $F(t)$ , presented in Fig. 7a, which reveals a sequence of small drops in  $F(t)$ . As in the experiments (e.g. Fig. 3), these force drops correspond to discrete rupture-like precursors to sliding which occur well below the onset of overall motion and result from a minute motion of the blocks at the slider's trailing edge (see Fig. 8).

What is the nature of the detachment fronts and their effect on the state of the system? In Fig. 7 we present both the stress distribution along the chain of blocks (Fig. 7b) and the fraction of detached contacts as functions of the block number and time (Fig. 7c). As in the experimental observations, we found that the onset of sliding is preceded by well-defined detachment fronts which are initiated at the trailing edge and extend over limited lengths across the slider which are smaller than its overall length. Figure 7b shows that these fronts generate a strongly nonuniform stress distribution across the interface. As a

result, a new detachment front will propagate into an already highly stressed region that has been prepared by the previous front. The new front easily ruptures the pre-stressed contacts in this region, further extends itself and causes further elastic deformation of the slider. The threshold values of the applied force corresponding to the detachment fronts are considerably lower than the value needed to initiate overall motion of the slider, because only regions of limited length are fractured during these precursor events.

As in the experimental observations, our simulations show that three different types of detachment fronts play a role in the onset of sliding: (1) sub-Rayleigh (limited by the Rayleigh wave speed) fronts, (2) slow detachment fronts, and (3) super-shear (or "intersonic") fronts that propagate at speeds beyond the shear wave speed. The velocities of the detachment fronts found in simulations are given by the slopes of the fronts shown in Figs. 7c, d and 10c, d. In these figures the slopes are in units of number of blocks per unit time. In order to obtain the values of velocities, one has to multiply these quantities by  $L/N$ . Thus, values of wave-velocities are well defined by simulations.

As a result of nonuniform loading, the precursors to sliding are always initiated at the trailing edge by the sub-Rayleigh front that rapidly accelerates until approaching the sound velocity,  $V \propto \sqrt{K/M}$ . This front is characterized by the simultaneous motion of a number of blocks which are detached from the base. Therefore, the velocity of the front,  $V$ , is determined by the elasticity of the slider and is independent of both the stiffness and rupture thresholds of the surface contacts. The properties of the contacts influence the number of blocks (of the slider domain) involved in a simultaneous motion, and the local displacements of the blocks. These decrease with the ratio between the stiffnesses of the surface contacts and the slider,  $K_s/K$  (see Fig. 7). Figure 7 also shows that, during transition to sliding, the blocks perform stick-slip motion where slips correspond to the precursor events, and the slip lengths are in the micrometer range.

Once the sub-Rayleigh front extends beyond the highly stressed region, it arrests. At the tip of the arrested front, however, a high excess stress is retained. This stress focusing is expected at the tip

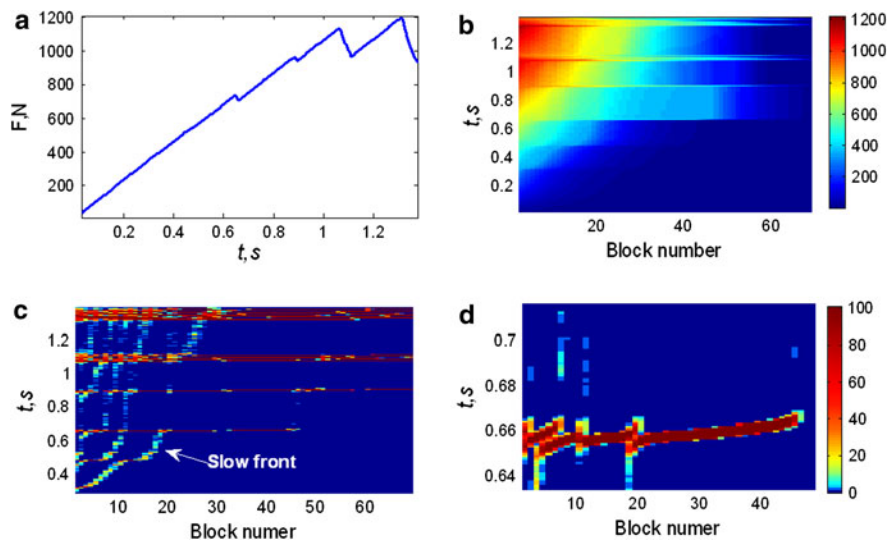


Figure 7

Onset of sliding for soft surface contacts,  $K_s = K$ . **a** A loading curve,  $F(t)$ . **b, c** Present color maps for the distribution of elastic forces,  $K(N - 1)(x_j - x_{j-1})$  in the slider and the percent of detached contacts as functions of the block number,  $j$ , and time,  $t$ . **d** An enlarged view of the fast detachment front from **c** showing an excitation of a secondary sub-Rayleigh front by the slow fronts. The unstressed and stressed regions (**b**) and the regions with attached and detached contacts (**c, d**) are displayed by *blue* and *red* colors, respectively. The *bars* to the *right* of the maps set up a correspondence between the colors and the values of the force in Newtons (**b**), and the fraction of detached contacts in % (**c**)

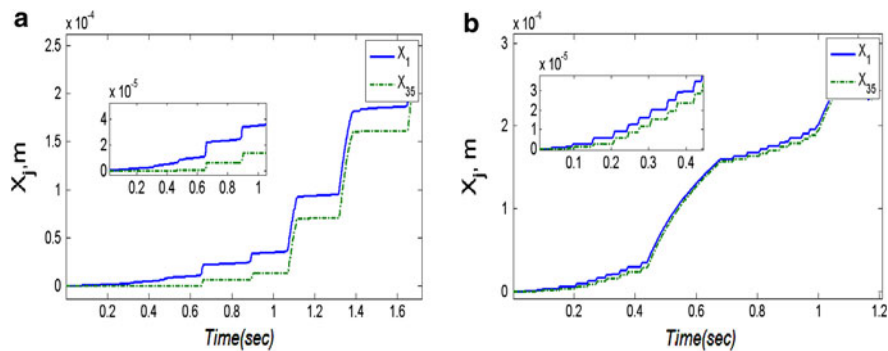


Figure 8

*Color on line* displacements of the first block,  $x_1$  (trailing edge) and the middle block,  $x_{35}$ , as a function of time for the case of soft (**a**) and stiff (**b**) surface contacts. *Insets* present enlarged views of the motion of blocks prior to the onset of overall sliding

of an arrested rupture. The accumulation of stress is clearly seen in Fig. 9, where we present a 2D map for the stress distribution in the surface contacts as function of the block number and time. Here we show the average force experienced by contacts connecting a given block  $j$  to the base,  $f_j = \frac{1}{N_s} \sum_i^{N_s} f_i^{(j)}$ , where  $f_i^{(j)} = k_i^{(j)} l_i^{(j)}$ ,  $l_i^{(j)}(t)$  is the contact elongation, and the averaging is taken over all contacts corresponding to the same block  $j$ . This excess stress triggers a slow detachment front that is similar to those observed

experimentally (e.g. Fig. 4a, bottom). As in the experiments, these slow fronts propagate with a velocity that is over an order of magnitude lower than  $V_R$  (see Figs. 7c, 9). In contrast to the sub-Rayleigh fronts, which exhibit the collective motion of the detached blocks, the slow fronts represent the motion of individual blocks. At each moment only one or a few blocks become partially detached from the base and move. As a result, the velocity of the slow front is determined mostly by the frictional properties of the

individual blocks (stiffness of surfaces contacts, thresholds of rupture forces) and depends only slightly on the slider elasticity. In particular, the velocity decreases with the increase in interfacial stiffness,  $K_s$ , and mean rupture force,  $F_s$ .

Figures 7c, d show that the interaction between the sub-Rayleigh front propagating from the trailing edge and the slow fronts triggers the excitation of secondary sub-Rayleigh fronts at various distances from the edge. This effect leads to a formation of a new type of fast fronts which corresponds to a superposition of sub-Rayleigh fronts which are initiated simultaneously at different locations across the slider. An effective velocity of such fast fronts can be a few times higher than  $V_R$ . These “chained” fronts may be analogous to the super-shear (inter-sonic) detachment fronts that have been observed experimentally (RUBINSTEIN *et al.*, 2004, 2007), under the loading conditions noted in Figs. 1 and 2, as well as under either impact loading conditions from the system’s edge (ROSAKIS *et al.*, 1999, 2000) or loading conditions for which fronts were triggered explosively (XIA *et al.*, 2004). This overall scenario for super-shear rupture may be rather general, as finite element simulations (NEEDLEMAN, 1999) performed for the case of shear fracture under impact loading (ROSAKIS *et al.*, 1999, 2000) suggest a similar

scenario, in which the transition to super-shear rupture involves micro-crack nucleation ahead of the main rupture front.

Figure 7b demonstrates that with each successive detachment front, the stress distribution across the slider becomes increasingly more nonuniform. By the time the system is ready to slide, the precursor fronts have generated highly stressed states of the slider and the contacts. Hence, the transition to sliding occurs in the highly nonuniform, stressed system. The transition to sliding is manifested by a significant drop in the loading curve,  $F(t)$ , which is an order of magnitude larger than the small drops corresponding to precursors of sliding. Contrary to the precursors which are caused by the discrete detachment fronts, the transition to overall sliding occurs through a quasi-continuous (in time) set of fronts propagating one after another from the trailing to the leading edges of the slider. During the time interval corresponding to this transition, most surface contacts are simultaneously detached and, therefore, allow the overall motion of the slider.

It is notable that for a system with moderately flexible surface contacts ( $K_s \approx K$ ) the nonuniform stress distribution produced by the sequence of detachment fronts prior to the first sliding event remains virtually unchanged in the subsequent stick-slip motion. This result is consistent with experimental observations (RUBINSTEIN *et al.*, 2007) which suggested that, under edge loading conditions, non-uniformity of the contact is the preferred state of the system during sliding.

Our calculations demonstrate that dynamics of the transition to sliding depend on the material properties. For instance, for stiff surface contacts with  $K_s = 50 K$  the slow fronts do not evolve, since in this case the excess stress accumulated at the tip of the arrested sub-Rayleigh front cannot overcome the resistance of the surface contacts and initiate slow motion (see Fig. 10). As a result, in this case we also did not find the super-shear fronts (see Figs. 10b, d), and the onset of sliding is completely determined by the propagation of the sub-Rayleigh fronts. Another distinctive property of a surface with stiff contacts is a release of high stresses in the slider and renewal to nearly a uniform stress state that is precipitated by sliding. The difference in stress relaxation during the

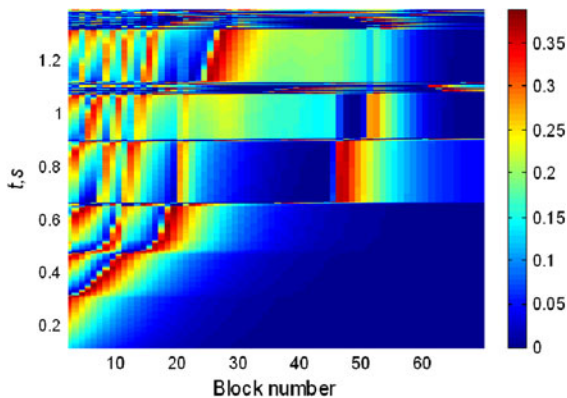


Figure 9

Color map for the distribution of elastic forces,  $f_j = \frac{1}{N_s} \sum_i^{N_s} f_i^{(j)}$ , in the contacts as functions of the block number,  $j$ , and time,  $t$ . The unstressed and stressed regions are displayed by blue and red colors, respectively. As in Fig. 7, these simulations were performed for  $K_s \sim K$ . The bar to the right of the maps set up a correspondence between the colors and the values of the force in Newtons

stick–slip transition leads to a very different mechanism of stick–slip motion for soft and stiff surface contacts. In the case of soft contacts the second and subsequent stick–slip events occur at the pre-stressed interface and do not involve a sequence of rupture-like precursors (see Figs. 7, 8). This scenario is similar to the experimental observations.

In the case of stiff contacts where the stress is relieved by sliding, all stick–slip transitions occur through the excitation of discrete detachment fronts (see Figs. 8b, 10). Thus dynamics of transition from static to kinetic friction strongly depend on the ratio between the stiffnesses of the surface contacts and the slider,  $K_s/K$ .

#### 4. Discussion

These experiments and simulations suggest an intuitive picture for the sequence of events leading to frictional sliding when shear is applied to the edge of a system. Recent experimental observations have demonstrated that the local stress profiles can have a dominant effect on how ruptures along a frictional interface are generated (BEN-DAVID *et al.*, 2010a). Depending on the initial stress profile along an

interface, a variety of different types of rupture modes and rupture sequences can be triggered (BEN-DAVID *et al.*, 2010a).

Here we have demonstrated that when shear forces are applied so as to create a nonuniform shear gradient near a pinned edge, the following detailed sequence of events occurs: before the onset of slip, the loading at the trailing edge imposes a high shear stress region near the edge, whose magnitude decays over a typical length that is proportional to  $h$ . When  $F_s$  is sufficiently large, this highly stressed region yields and an initial slip event is generated. The slip traverses this region and arrests at a distance,  $l_0$ , where the shear stress level is below the slipping threshold. This event results in: (1) slip within the region  $l_0$ , where built-up shear stresses are released, (2) elastic deformation of the slider to compensate for the slip-induced contraction in the  $x$  direction. The deformation results in an outwardly protruding region of size  $D \sim 1/3l_0$  in which the contact area increases, thereby dynamically forming an asperity (cf. Figure 6a). The inwardly bowed region over the remainder of the region  $l_0$ , reduces the normal force [equivalent to a decrease of  $A(x, t)$ ] (3) establishment of a high residual shear stress concentration entrained in the vicinity of the point of arrest of the slip event

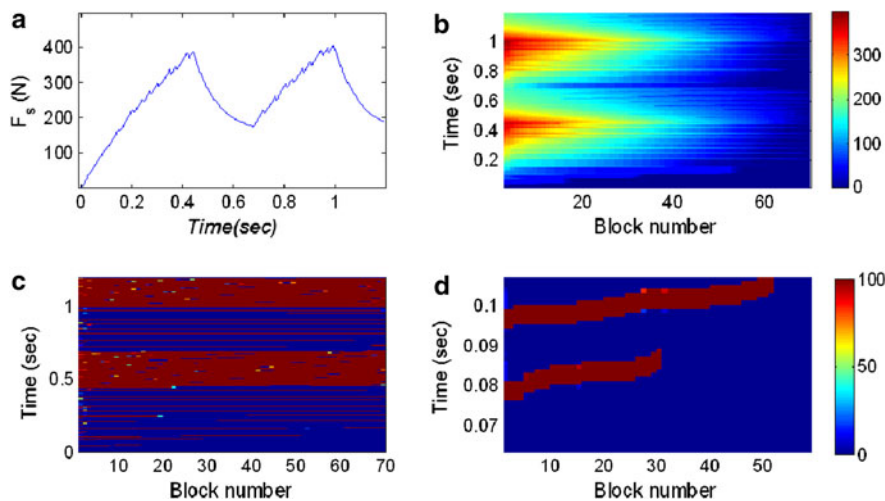


Figure 10

Onset of sliding for stiff surface contacts,  $K_s = 50 K$ . **a** A loading curve,  $F(t)$ . **b**, **c** Color maps for the distribution of elastic forces,  $K(N - 1)(x_j - x_{j-1})$  in the slider and the fraction of attached contacts as functions of the block number,  $j$ , and time,  $t$ . **d** An enlarged view of the detachment front from **c** showing a propagation of a sub-Rayleigh front. The notation is as in Fig. 7

(This is due to the stress singularity that occurs at the tip of a shear crack.). Upon further increase of  $F_S$ , the barrier imposed by the asperity is again overcome and a new slip event is generated. This slip event will easily traverse the weakened region beyond the asperity. Arriving at the tip of the previously arrested front, the new slip event will add sufficient energy to release the energy stored within the high-stress region imposed previously, thereby enabling it to extend itself by  $\Delta l$ . This extension is accompanied by further elastic deformation of the block, thereby increasing the nonuniformity of  $A(x, t)$ . In this way, each slip event transfers the shear stress imposed at the boundary further along the interface.

The influence of fault complexity on the dynamics of rupture propagation and seismicity has been the subject of intensive past and recent research (AKI, 1979; DAS, 2003; LAY *et al.*, 1982). Our experiments suggest that the fingerprint of an ‘edge’ can be traced, not only to the dynamics of a given rupture, but throughout the entire seismic cycle of a given fault. The results suggest that a geometrical inhomogeneity introduces a scale that may govern the nucleation, size and repeatability of earthquakes along a given fault.

It is interesting that ruptures precursory to periodic system-wide events were also observed in numerical studies (LAPUSTA and RICE, 2003) of faults driven by anti-plane shear in which both stress nonuniformity (via frictional properties that varied with fault depth) and a length scale (a critical earthquake nucleation size) were imposed. As in our studies, the number of the precursory events increased as the length scale decreased and, when the imposed length scale surpassed the system size (LAPUSTA *et al.*, 2000), the precursory ruptures were not observed and the system simply exhibited periodic stick–slip events over the entire system size. The work presented here differs from these earlier studies in both the mode of loading (in-plane shear) and that the stress nonuniformity and length scale are simply provided by the loading geometry. Nevertheless, it may be possible that the simple existence of nonuniform stress along a fault together with the existence of a length scale that is significantly smaller than fault dimensions could be sufficient to generate sequences of precursory events.

The experiments and model presented here paint an interesting picture of earthquake dynamics along faults that are loaded at an edge or a step. They indicate that stress transfer along such faults may be mediated by a periodic sequence of precursory events. This sequence of slip events culminates by the triggering of a slowly propagating front which leads to system-size events. The experiments suggest that the early slip events of the periodic sequence (within the scaling regime shown in Fig. 5a) “feel” an effectively infinitely long (unsegmented) fault. In contrast, the accelerated growth of  $l$  that marks the breakdown of scaling prior to the onset of large events indicates that the dynamics are affected by the fault size during the nucleation phase (OHNAKA and SHEN, 1999) of a large event. This accelerated increase in  $l$  is strongly suggestive of the accelerated seismic release that precedes some large earthquakes (BUFE and VARNES, 1993). The results also imply that precursory sequences of events that initiate from a fault edge strongly modify the fault contact plane prior to a large event.

One example of such slip sequences along a fault edge in the crust is portrayed by the foreshock sequence of the 1998 Sendai Bay event along the Nagamachi-Rifu fault, Japan (UMINO *et al.*, 2002). In this field case, the main shock of M5.0 was preceded by 17 foreshocks ranging in magnitude from 1.7 to 3.8 with essentially identical seismic characteristics. The foreshocks sequence lasted about 3 days with the largest foreshock occurring 6 min prior to the main shock. Mechanical modelling of this sequence of events suggests that the fault was edge-loaded by non-seismic slip in the lower crust (NAKAJIMA *et al.*, 2006). Accordingly, the foreshock hypocenters propagated upward along the locked part of the Nagamachi-Rifu fault. Finally, UMINO *et al.* noted that “A small ambiguous phase...is observed in seismograms of both the M5.0 main shock and the M3.8 largest foreshock...” (UMINO *et al.*, 2002). This slow, low amplitude ambiguous phase is lacking in the other foreshocks and all aftershocks, and is possibly the equivalent of the slow fronts observed in our experiments immediately before the main slip event (Figs. 4a, 7). These slow fronts may also relate to the accelerated creep events that are anticipated to be part of the nucleation phase of major earthquakes

(DIETERICH and KILGORE, 1996; OHNAKA and SHEN, 1999). Thus, in spite of scale and complexity differences, we note the following similarities between the 1998 Sendai Bay events and our experiments and simulations: (1) qualitatively similar (edge) loading conditions, (2) a distinct sequence of precursory events; (3) initiation of precursory events from nearly the same location and (4) a slow (“ambiguous”) phase that occurs only before the main event.

Another outstanding example of a sequence of foreshocks is the sequence of events that preceded the 1995 Mw 7.9 off-Etorofu earthquake, Kurile Islands (HURUKAWA, 1998). We show below that our experimental results can serve as laboratory analog for the foreshock-mainshock sequence of this earthquake. HURUKAWA (1998) relocated the foreshocks, the mainshock, and aftershocks, and used quality criteria (e.g., number of recording stations, minimum magnitude and distance, and low standard error), to analyze a total of 238 events. These events occurred along a 14°–19° dipping thrust of the boundary between the North American and Pacific plates (Fig. 11a). A series of 51 foreshocks initiated 9 days before the mainshock, including three events of  $M > 6$ . The foreshock area extended from depths greater than 40 km in the direction of the trench axis (Fig. 11b), with the final area covered by foreshock activity roughly  $80 \times 30$  km in size (Fig. 11c). The mainshock rupture initiated at the deepest point of the foreshock area, and its final area, as determined from aftershock distribution, was roughly six times the final area of the foreshock distribution (Fig. 11c).

We believe that the above observations of HURUKAWA (1998) may be analogous to the present experiments. This statement is based on the following similarities:

#### 4.1. Edge-loading

In the experiments, the laboratory “fault” was loaded by a continuously increasing force,  $F_S$ , at its edge (c.f. Fig. 1). In the field, the upper, brittle, locked part of the Kurile Islands thrust at shallow depths  $< 50$  km (black, inclined line in Fig. 11a), was loaded by its deeper, ductile, creeping part at depths  $> 50$  km (blue inclined line in Fig. 11a and blue area in Fig. 11b).

#### 4.2. Space–time Progression of Slip Events

In each experimental run, a series of arrested events propagated from the loading edge and extended the length of the slipped region (Fig. 3). This series of arrested events was culminated by an un-arrested event along the entire block (Fig. 3). We regard this event as the analog of a mainshock. In the off-Etorofu events, the foreshocks initiated in the deepest part of the brittle fault and propagated southeastward (above and Fig. 11b). As in the experiments, the mainshock also initiated at the loaded edge (the deepest part), covered the foreshock area and extended laterally (Fig. 11c).

#### 4.3. Increase of the Affected Length (Area)

Both the experiments and the field display systematic temporal increase of the affected length (along experimental fault, c.f. Fig. 3 and 5) or affected area (Kurile Islands thrust, Fig. 11c). This temporal progression is presented in Fig. 12 for the normalized values of length (area) and time. For the experiments, the normalized affected length is the ratio between the length of the arrested event, ( $l$  in Fig. 4) and the length of the un-arrested event ( $L$  is length of the experimental fault shown in Fig. 1). For the field data, the normalized affected length is  $\sqrt{A_F/A_M}$  where  $A_F$  is the area affected by the foreshocks at a given time, and  $A_M$  is the area of the mainshock; both  $A_F$  and  $A_M$  were determined from Fig. 11c, which is the model of Hurukawa (c.f. Fig. 8 in HURUKAWA, 1998). We use the square root of the area ratio to facilitate a comparison between area in the field and length in the experiments. The normalized time is  $t_n = (t - t_0)/\Delta t$ , where  $t$  is the time of the event (experimental or foreshock),  $t_0$  is the time of the first event, and  $\Delta t$  is the time difference between the first event and the last. For the experiments, we use the results of three runs loaded by similar rates but under different normal stresses.

Figure 12 displays general similarities between the time-progression of the arrested events in the experiments and the foreshocks of the 1995 Mw 7.9 off-Etorofu earthquake. In both settings, the length,  $l$ , (area) systematically increases with time for almost the entire duration of the sequence, until reaching

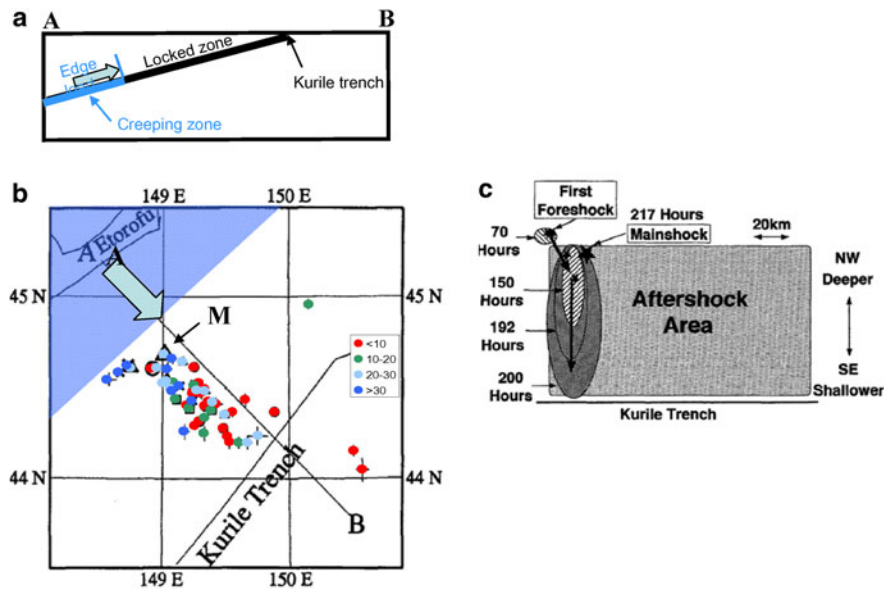


Figure 11

The foreshock sequence of the 1995, M7.9 off-Etorofu earthquake, Kurile trench; data from (HURUKAWA, 1998). **a** A schematic 2D model of the Kurile subduction zone in the area of the earthquake; the fault dips  $12^{\circ}$ – $19^{\circ}$  to the NW (HURUKAWA, 1998). We suggest that the upper, locked part of the fault (black line) is edge-loaded by the creeping lower part (blue). **b** Map of relocated foreshocks and mainshock (modified Fig. 5b in HURUKAWA, 1998). Events are divided into four depth groups marked in color (legend in km). The area in blue in the NW corner is the creeping zone according to the model in **a**; *M* denotes the mainshock. **c** Figure 8 from HURUKAWA, (1998) showing a schematic distribution of the foreshock activity (see text). The arrows show the dominant propagation direction. Note that the mainshock hypocenter is at the deepest edge of the foreshock area; stars represent magnitude 6 or larger earthquakes

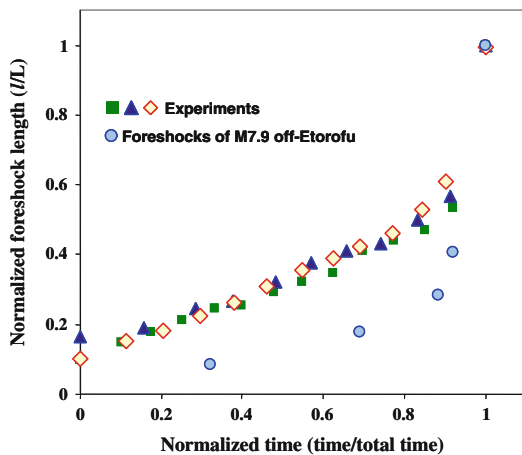


Figure 12

Time-progression of arrested slip events in three typical experiments (square, triangle, diamond symbols) of the present study and in the foreshock sequence (circles) of the 1995, M7.9 off-Etorofu earthquake, Kurile trench. The latter data were obtained from Fig. 11c (Fig. 8 in HURUKAWA, 1998) and modified, as explained in the text. The linear temporal dependence in the experimental data reflects the constant forcing rate used in the experiments. The forcing rate in the Etorofu events is the (unknown) creep rate at depths over 50 km. This may be the reason that the field data exhibit nonlinear temporal dependence of the foreshock sequence

approximately 40–45% of the final length,  $L$  (area).  $L$  is analogous to the additional length (area) is covered during the mainshock in the field. In the figure, the linear progression of  $l$  in the experiments is due to the linear increase with time of the applied shear force,  $F_S$ . In the Etorofu sequence, we do not know whether the creep (edge-loading) rate was constant over the duration of the foreshock sequence. If so, we would expect the same quasi-linear temporal increase of the event sizes.

We speculate that the general similarities between the experimental sequences of slip event and the seismic foreshock sequences of off-Etorofu and Sendai earthquakes are not coincidental. While certainly not the only explanation (BEN-ZION and LYAKHOVSKY, 2002), we believe that this similarity reflects the effect of edge-loading on a locked fault and event progression that is needed to weaken the locked segment and to prepare it for the mainshock. As both our model and experiments show, the qualitative (generic) form imbued in edge-loading is *sufficient* to trigger this general sequence of events.

We, therefore, expect that a locked fault segment which is edge-loaded by a deep, creeping segment, e.g. in subduction zones, could fail in a mode similar to our experiments.

In conclusion, the results of this study have shown that the fact that shear is applied nonuniformly to a sliding system leads to complex, systematic behaviour that appears analogous to natural phenomena whose sources are currently not well understood. We believe that the analogies between our experimental results and seismic observations stem from their similar edge-loading configurations. As edges and bumps are common in faults at many scales (SAGY *et al.*, 2007; STEIN *et al.*, 1997), it is therefore anticipated that this loading will generate stress distributions that are similar to the laboratory model and, consequently, may lead to similar dynamics.

#### Acknowledgments

S. M. R. and J. F. acknowledge the support of grant no. 2006288 awarded by the U.S.-Israel Binational Science Foundation. This work, as part of the ESF EUROCORES programme FANAS, was supported by the Israel Science Foundation. J. F. acknowledges the support of the Max Born chair of Natural Philosophy. Z. R. received support from NSF Continental Dynamics grant No. 0409605 (NELSAM). M.U. acknowledges the support of the DIP grant.

#### REFERENCES

- AAGAARD B.T., and HEATON, T.H., (2004), *Near-source ground motions from simulations of sustained intersonic and supersonic fault ruptures*: Bulletin of the Seismological Society of America, v. 94, p. 2064–2078.
- AKI K., (1979), *Characterization of Barriers on an Earthquake Fault*: Journal of Geophysical Research, v. 84, p. 6140–6148.
- ALAVA M.J., NUKALAZ, P., and ZAPPERI, S., (2006), *Statistical models of fracture*: Advances in Physics, v. 55, p. 349–476.
- BAREL I., URBAKH, M., JANSEN, L., and SCHIRMEISEN, A., (2010), *Multibond Dynamics of Nanoscale Friction: The Role of Temperature*: Physical Review Letters, v. 104, p. 066104.
- BEN-DAVID O., COHEN, G., and FINEBERG, J., (2010a), *The dynamics of the onset of frictional slip*: Science, v. 330, p. 211–214.
- BEN-DAVID O., RUBINSTEIN, S.M., and FINEBERG, J., (2010b), *Slip-stick and the evolution of frictional strength*: Nature, v. 463, p. 76–79.
- BEN-ZION Y., and LYAKHOVSKY, V., (2002), *Accelerated Seismic Release and Related Aspects of Seismicity Patterns on Earthquake Faults*: Pure Appl. Geophys., v. 159, p. 2385–2412.
- BEN-ZION Y., and SAMMIS, C.G., (2003), *Characterization of fault zones*: Pure and Applied Geophysics, v. 160, p. 677–715.
- BRAUN O.M., BAREL, I., and URBAKH, M., (2009), *Dynamics of Transition from Static to Kinetic Friction*: Physical Review Letters, v. 103, p. 194301.
- BRAUN O.M., and PEYRARD, M., (2008), *Modeling friction on a mesoscale: Master equation for the earthquakelike model*: Physical Review Letters, v. 100, p. 125501.
- BRAUN O.M., and RÖDER, J., (2002), *Transition from stick-slip to smooth sliding: An earthquakelike model*: Physical Review Letters, v. 88, p. 096102.
- BRAUN O.M., and TOSATTI, E., (2009), *Kinetics of stick-slip friction in boundary lubrication*: Epl, v. 88, p. 48003.
- BUFE C.G., and VARNES, D.J., (1993), *Predictive Modeling of the Seismic Cycle of the Greater San-Francisco Bay-Region*: Journal of Geophysical Research-Solid Earth, v. 98, p. 9871–9883.
- BURRIDGE R., and KNOPOFF, L., (1967), *Model and Theoretical Seismicity*: Bulletin of the Seismological Society of America, v. 57, p. 341.
- CARLSON J.M., and LANGER, J.S., (1989), *Properties of Earthquakes Generated by Fault Dynamics*: Physical Review Letters, v. 62, p. 2632–2635.
- DAHMEN K.A., BEN-ZION, Y., and UHL, J.T., (2009), *Micromechanical Model for Deformation in Solids with Universal Predictions for Stress-Strain Curves and Slip Avalanches*: Physical Review Letters, v. 102, p. 175501.
- DAS S., (2003), *Spontaneous complex earthquake rupture propagation*: Pure and Applied Geophysics, v. 160, p. 579–602.
- DIETERICH J.H., and KILGORE, B., (1996), *Implications of fault constitutive properties for earthquake prediction*: Proceedings of the National Academy of Sciences of the United States of America, v. 93, p. 3787–3794.
- DIETERICH J.H., and KILGORE, B.D., (1994), *Direct Observation of Frictional Contacts - New Insights for State-Dependent Properties*: Pure and Applied Geophysics, v. 143, p. 283–302.
- FILIPPOV A.E., KLAFTER, J., and URBAKH, M., (2004), *Friction through dynamical formation and rupture of molecular bonds*: Phys Rev Lett, v. 92, p. 135503.
- HARRIS R.A., and DAY, S.M., (1993), *Dynamics of Fault Interaction - Parallel Strike-Slip Faults*: Journal of Geophysical Research-Solid Earth, v. 98, p. 4461–4472.
- HURUKAWA N., (1998), *The 1995 Off-Etorofu Earthquake: Joint Relocation of Foreshocks, the Mainshock, and Aftershocks and Implications for the Earthquake Nucleation Process*: Bull. Seismol. Soc. Am, v. 88, p. 1112–1126.
- JOHNSON A.M., FLEMING, R.W., and CRUIKSHANK, K.M., (1994), *Shear Zones Formed Along Long, Straight Traces of Fault Zones During the 28 June 1992 Landers, California, Earthquake*: Bulletin of the Seismological Society of America, v. 84, p. 499–510.
- LACHENBRUCH A.H., and SASS, J.H., (1980), *Heat-Flow and Energetics of the San-Andreas Fault Zone*: Journal of Geophysical Research, v. 85, p. 6185–6222.
- LANDAU L.D., and LIFSHITZ, E.M., 1986, *Theory of Elasticity*, New York, Pergamon.
- LAPUSTA N., and RICE, J.R., (2003), *Nucleation and early seismic propagation of small and large events in a crustal earthquake*

- model*: Journal of Geophysical Research-Solid Earth, v. 108, p. 2205.
- LAPUSTA N., RICE, J.R., BEN-ZION, Y., and ZHENG, G.T., (2000), *Elastodynamic analysis for slow tectonic loading with spontaneous rupture episodes on faults with rate- and state-dependent friction*: Journal of Geophysical Research-Solid Earth, v. 105, p. 23765–23789.
- LAY T., KANAMORI, H., and RUFF, L., (1982), *The Asperity Model and the Nature of Large Subduction Zone Earthquakes*: Earthquake Prediction Research, v. 1, p. 3–71.
- MAEGAWA S., SUZUKI, A., and NAKANO, K., (2010) *Precursors of Global Slip in a Longitudinal Line Contact Under Non-Uniform Normal Loading*: Tribology Letters, v. 38, p. 313–323.
- MATSUURA M., and SATO, T., (1997), *Loading mechanism and scaling relations of large interplate earthquakes*: Tectonophysics, v. 277, p. 189–198.
- NAKAJIMA J., HASEGAWA, A., HORIUCHI, S., YOSHINOTO, K., YOSHIDE, T., and UMINO, N., (2006), *Crustal heterogeneity around the Nagamachi-Rifu fault, northeastern Japan, as inferred from travel-time tomography*: Earth Planets and Space, v. 58, p. 843–853.
- NEEDLEMAN A., (1999), *An analysis of intersonic crack growth under shear loading*: Journal of Applied Mechanics-Transactions of the Asme, v. 66, p. 847–857.
- NIELSEN S., TADDEUCCI, J., and VINCIGUERRA, S., (2010), *Experimental observation of stick-slip instability fronts*: Geophysical Journal International, v. 180, p. 697–702.
- OHNAKA M., and SHEN, L.F., (1999), *Scaling of the shear rupture process from nucleation to dynamic propagation: Implications of geometric irregularity of the rupturing surfaces*: Journal of Geophysical Research-Solid Earth, v. 104, p. 817–844.
- OLAMI Z., FEDER, H.J.S., and CHRISTENSEN, K., (1992), *Self-Organized Criticality in a Continuous, Nonconservative Cellular Automaton Modeling Earthquakes*: Physical Review Letters, v. 68, p. 1244–1247.
- PERSSON B.N.J., (1995), *Theory of Friction - Stress Domains, Relaxation, and Creep*: Physical Review B, v. 51, p. 13568–13585.
- RECHES Z., SCHUBERT, G., and ANDERSON, C., (1994), *Modeling of Periodic Great Earthquakes on the San-Andreas Fault - Effects of Nonlinear Crustal Theology*: Journal of Geophysical Research-Solid Earth, v. 99, p. 21983–22000.
- RICE J.R., and BEN-ZION, Y., (1996), *Slip complexity in earthquake fault models*: Proceedings of the National Academy of Sciences of the United States of America, v. 93, p. 3811–3818.
- ROSAKIS A.J., SAMUDRALA, O., and COKER, D., (1999), *Cracks faster than the shear wave speed*: Science, v. 284, p. 1337–1340.
- ROSAKIS A.J., SAMUDRALA, O., and COKER, D., (2000), *Intersonic shear crack growth along weak planes*: Materials Research Innovations, v. 3, p. 236–243.
- RUBINSTEIN S.M., COHEN, G., and FINEBERG, J. (2004), *Detachment fronts and the onset of dynamic friction*: Nature, v. 430, p. 1005–1009.
- RUBINSTEIN S.M., COHEN, G., and FINEBERG, J., (2007), *Dynamics of precursors to frictional sliding*: Physical Review Letters, v. 98, p. 226103.
- RUBINSTEIN S.M., COHEN, G., and FINEBERG, J., (2008), *Cracklike Processes within Frictional Motion: Is Slow Frictional Sliding Really a Slow Process?*: MRS Bulletin, v. 33, p. 1181–1189.
- RUBINSTEIN S.M., COHEN, G., and FINEBERG, J., (2009), *Visualizing stick-slip: experimental observations of processes governing the nucleation of frictional sliding*: Journal of Physics D-Applied Physics, v. 42, p. 214016.
- RUBINSTEIN S.M., SHAY, M., COHEN, G., and FINEBERG, J., (2006), *Crack like processes governing the onset of frictional slip*: Int. J. of Fracture, v. 140, p. 201–212.
- SAGY A., BRODSKY, E.E., and AXEN, G.J., (2007), *Evolution of fault-surface roughness with slip*: Geology, v. 35, p. 283–286.
- SHAW B.E., and DIETERICH, J.H., (2007), *Probabilities for jumping fault segment stepovers*: Geophysical Research Letters, v. 34, p. L01307.
- STEIN R.S., BARKA, A.A., and DIETERICH, J.H., (1997), *Progressive failure on the North Anatolian fault since 1939 by earthquake stress triggering*: Geophysical Journal International, v. 128, p. 594–604.
- TSAMADOS M., TANGUY, A., LEONFORTE, F., and BARRAT, J.L., (2008), *On the study of local-stress rearrangements during quasi-static plastic shear of a model glass: Do local-stress components contain enough information?*: European Physical Journal E, v. 26, p. 283–293.
- UMINO N., OKADA, T., and HASEGAWA, A., (2002), *Foreshock and aftershock sequence of the 1998 M 5.0 Sendai, northeastern Japan, earthquake and its implications for earthquake nucleation*: Bulletin of the Seismological Society of America, v. 92, p. 2465–2477.
- WESNOSKY S.G., (2006), *Predicting the endpoints of earthquake ruptures*: Nature, v. 444, p. 358–360.
- XIA K.W., ROSAKIS, A.J., and KANAMORI, H., (2004), *Laboratory earthquakes: The sub-Rayleigh-to-supershear rupture transition*: Science, v. 303, p. 1859–1861.